International Journal of Concrete Structures and Materials

RESEARCH Open Access

Experimental Study on Structural Performance of Cast-in-Place Frame Printed Concrete Wall

Yanan Fu[1], Ying Zhang[1] and Lei Wu[1*]

Abstract

A growing number of nations and regions have printed concrete structures thanks to the application of 3D printing technology in the field of civil engineering. However, the houses built with printed concrete are mostly printed concrete wall structures with composite load-bearing walls and cast-in-place frames. This structure solely takes into account the performance of the structure under vertical loads, which does not address its ability to withstand horizontal loads. In this paper, wall specimens were designed and tested under horizontal reciprocal loads in order to investigate the structural performance of this cast-in-place border-frame printed concrete wall structure under horizontal loads. Four factors are examined in order to determine how well the cast-in-place frame printed concrete wall structure performs when subjected to horizontal loads: column longitudinal reinforcement strain, hysteresis curve, skeleton curve, and energy dissipation capacity. According to the test results, the addition of the wall increased the bearing capacity and accumulated energy dissipation of the specimen, but the increase in stiffness also caused the structural ductility to decrease. As a result, cracks were more likely to generate at the wall–column joints, so the stiffness matching between the printed concrete wall and the cast-in-place side frame needed to be further coordinated to obtain a higher ductility. It turns out that the wall sections have little impact on the seismic performance of the members.

Keywords 3D-printed concrete, Cast-in-place frame, Wall, Horizontal reciprocal load test

1 Introduction

The usage of 3D printing technology in the construction of houses, which has attributes of automation, information technology, and intelligence, is growing in the context of worldwide industrial growth towards automation and digitalization. A residential building with one floor underground and five floors above ground was printed by Shanghai WinSun at Suzhou Industrial Park in 2015 to become the world's tallest 3D-printed building (Alec, 2016; Yu, 2015, 02). In 2016, Dubai manufactured an office building completely made of 3D printing in just 17 days (Koslow, 2016; Tess, 2016). The first officially habitable house in the world was constructed in 2021 at Eindhoven University of Technology in the Netherlands applying 3D-printed concrete technology. It is a bungalow with two bedrooms. This single-story residence and four more multi-story residences are part of their milestone project, all of which satisfy the needs of the residents in terms of comfort, layout, quality, and price (Frearson, 2018; Gallow, 2022; Keighran, 2022).

Related research has revealed that the aggregate gradation and components of concrete (Liu et al., 2019), the printing interval time (Panda et al., 2018) and the height of the nozzle from the printed layer all have an impact on the mechanical characteristics of 3D-printed

Journal information: ISSN 1976-0485 / eISSN 2234-1315.

*Correspondence:
Lei Wu
1293539197@qq.com
[1] School of Civil Engineering, Southeast University, Nanjing 211189, Jiangsu, China

concrete. Additionally, the accumulation forming technique used in 3D-printed concrete printing causes pores to emerge between the printing layers as the structure takes shape, leading to micro cracks. Since the internal forces of the printed concrete are varied, the mechanical properties of 3D-printed concrete components are anisotropic (Le et al., 2012, 3; Sanjayan et al., 2018; Zhang et al., 2021b, 1). As a result, quite a number of studies have been conducted to enhance the mechanical properties of printed concrete members. Reinforcement is frequently employed in 3D-printed concrete, with horizontal reinforcement being simpler and vertical reinforcement being more challenging. There are two types of reinforcement: manual reinforcement and automatic reinforcement (Zhang, 2020). The manual reinforcement occurs in the following situations: (1) vertical holes are reserved at both ends of the wall when the wall is printed, vertical reinforcement is inserted after the wall is printed, and concrete is filled in the holes after the concrete is hardened (Zhang et al., 2021a, 06). (2) Only the hollow wall is printed and the reinforcement cage is lifted at the location where the structural column is designed. The reinforcement cage can be welded to the foundation raw reinforcement by reserving welding holes at the bottom of the printed wall (Lin et al., 2021, 03). (3) With strategically placed reinforcing cages and plastic pipes, Chinese construction company Huashang Tengda prints concrete on the foundation (Molitch-Hou, 2016). In addition, some academics have utilized materials to print reinforcing bars or mixed in mortar to increase the strength of composites for vertical reinforcement purposes. The production of vertical bars with and without extra ribs using gas-metal arc welding 3D-printed reinforcing bars was proven to be feasible by Mechtcherine's feasibility research (Mechtcherine et al., 2018).

In recent years, the majority of the engineering practice of printing concrete construction of multi-story houses has adopted a construction method similar to a masonry structure, which entails first printing concrete wall elements and reserving cast-in-place concrete column connection section at the end of the wall at the same time, and setting cast-in-place beam section at the top of the wall and horizontal floor cover connected parts so as to form a wall and cast-in-place side frame composite load-bearing printing concrete wall structure. The structural ability of this construction to support horizontal loads is not given much consideration in its application; rather, it is primarily taken into account for its vertical load-bearing capability. In this paper, 3D-printed concrete wall specimens with cast-in-place reinforced concrete borders were modeled, designed, and tested for horizontal reciprocal loads to see how well the construction performed in resisting horizontal loads. The failure modes of the printed concrete specimens were compiled, the data on the reinforcement stresses and strains of the specimens were obtained, and the structural performance was examined from four angles: column longitudinal reinforcement strain, hysteresis curve, skeleton curve, and energy dissipation capacity.

2 Experimental Design

The majority of hollow walls are utilized in engineering practice to reduce the amount of concrete needed for printing and increase printing effectiveness. The test was designed to print a concrete hollow wall specimen with a cast-in-place frame (Specimen 1). To observe the impact of the stiffness of the printed concrete wall and the frame stiffness on the overall structure, a solid printed concrete wall structure with a frame (Specimen 2) and a frame structure (Specimen 3), respectively, were each designed and put through horizontal reciprocal loading tests for comparison.

2.1 Specimen Description

2.1.1 Hollow Printed Concrete Wall Specimen with Cast-in-Place Frame

Vertical printing was used to create the hollow walls. With HRB335-grade horizontal tie steel bars of 6 mm diameter, the printed hollow wall size has dimensions of 1480 mm × 1260 mm × 180 mm. Since the walls are printed in layers to create the components, tie bars are positioned when the walls are printed to a specific height. The horizontal tie bars are deeply embedded in the reinforcement cage of the frame column, and then the concrete of the frame part was poured, and when the maintenance is completed, the frame-print wall integral specimen is constructed. The tie bars, which are the equivalent of horizontal ties, both guarantee that the wall does not stop functioning by shifting out of the wall frame plane, and also provide a certain degree of tie capacity. The hollow wall cross-sectional drawing and physical drawing are shown in Fig. 1.

The cast-in-place frame column has a cross-sectional area of $b1 \times h1 = 240$ mm × 240 mm (where $b1$ is the width of the column section, $h1$ is the height of the column section), a total height of 1600 mm, and a distance of 1720 mm between the two columns. The cast-in-place frame beam has a cross-sectional area of $b2 \times h2 = 200$ mm × 240 mm and a total length of 2160 mm (where $b2$ is the width of the beam section, $h2$ is the height of the beam section). The cross-sectional size of the bottom beam for test anchorage is $b3 \times h3 = 400$ mm × 400 mm with an overall length of 2560 mm. Fig. 2 depicts the dimension of the wall frame with hollow print (where $b3$ is the width of the

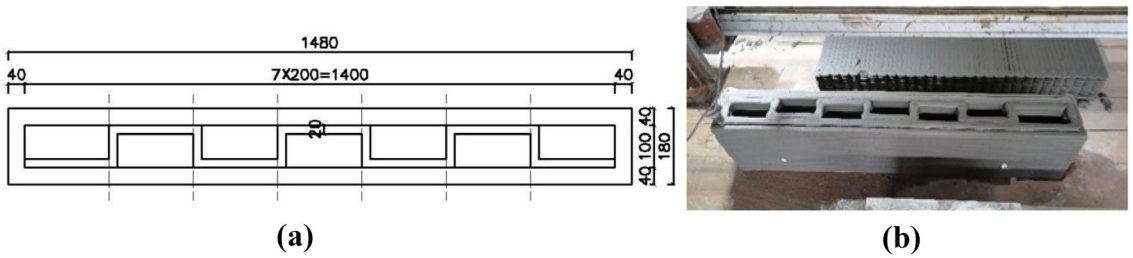

Fig. 1 Hollow wall diagram. **a** Schematic diagram of cross-section of hollow wall (mm). **b** Hollow wall physical drawing (mm)

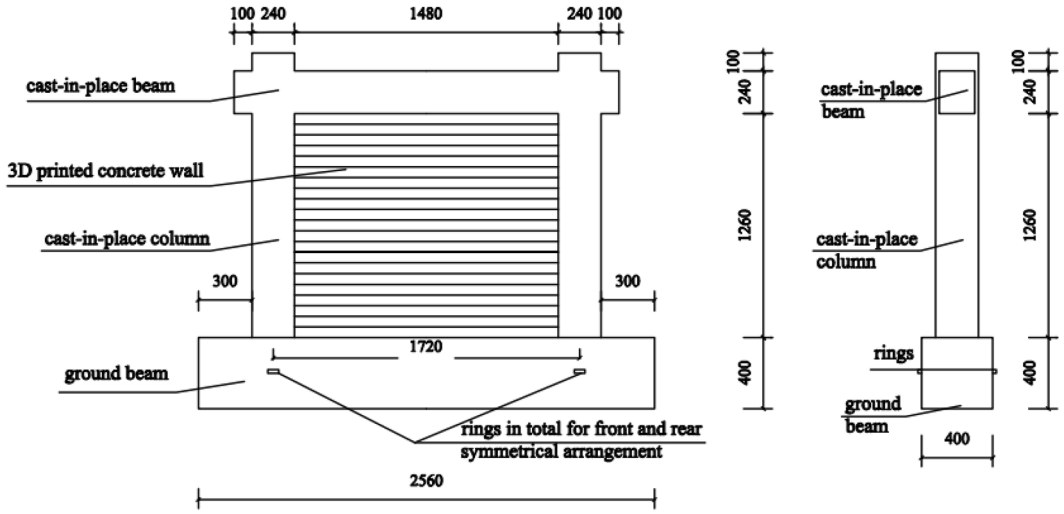

Fig. 2 Dimensions of wall frame with hollow printing (mm)

bottom beam section, $h3$ is the height of the bottom beam section).

The hoop and longitudinal bars of the cast-in-place frame column are HRB400 grade, with a 12-mm longitudinal bar diameter and an 8-mm hoop bar diameter. The longitudinal bars and hoop bars of the cast-in-place frame beam are HRB400 grade, with a 12-mm longitudinal bar diameter and an 8-mm hoop bar diameter. The hoop and longitudinal bars of the bottom beam for test anchorage are HRB400 grade, with a 20-mm longitudinal bar diameter and an 8-mm hoop bar diameter. The connection steel between the print wall and connection reinforcement between the print wall and the cast-in-place frame is HRB335 grade reinforcement with a 6 mm diameter. The cast-in-place frame is made of C35 concrete with a 25-mm concrete covering. Fig. 3 depicts the frame reinforcement. (The strength grades of steel bar and concrete refer to "code for design of concrete structure (GB 50010-2010)".)

2.1.2 Solid Concrete Wall Specimen with Cast-in-Place Frame

The printed solid wall dimensions and reinforcement are the same as the hollow printed wall. The physical drawing of the solid wall is shown in Fig. 4. The cast-in-place frame columns and beams are identical to those in Specimen 1 in terms of the dimensions and reinforcement. As the solid walls are formed by horizontal printing, tie bars are positioned when the walls are printed at a specific thickness. However, the solid walls were printed horizontally in order to lessen the distortion caused by self-weight, and the contact surface between the walls and the floor beams is trimmed once the printing is completed.

2.1.3 Specimen of Cast-in-Place Frame

Only the cast-in-place frame was kept, and the dimensions and reinforcement of the cast-in-place side frame columns and beams matched those in Specimen 1. Fig. 5 depicts the dimension of the frame, and Fig. 6 depicts the reinforcement of the cast-in-place frame.

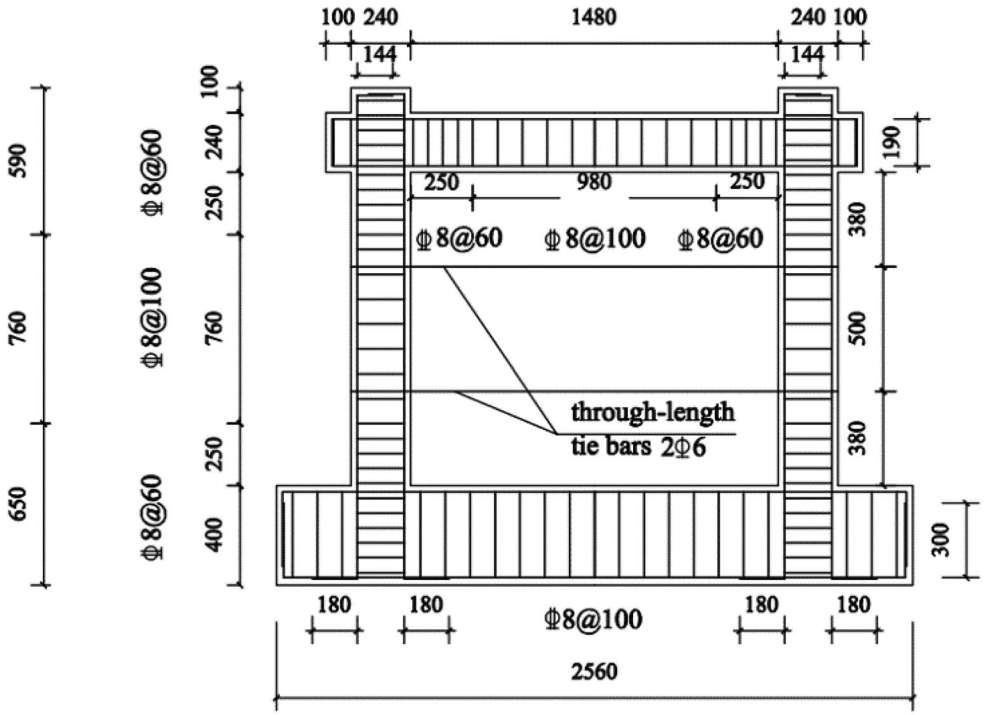

Fig. 3 Reinforcement of cast-in-place frame print concrete wall component (mm)

2.2 Test Loading Method

2.2.1 Testing Device

The MTS electro-hydraulic servo actuator system for the horizontal low-cycle repetitive load device has a displacement control capability of 1000 kN. A hydraulic jack is used to apply the axial pressure load while a steel compression beam and mechanical jack are used to fix the bottom beam. The uniform vertical load on the wall is equivalent to a concentrated force loaded on both ends of the component and the axial pressure load is transferred to the top of the side frame column through the loading beam. The wall has a very poor lateral capacity to withstand horizontal forces. In order to analyze the capacity of the structure to resist horizontal forces (seismic), the horizontal forces are added to the side of the wall frame with reference to the analysis of the seismic performance of the shear wall structure. The TST3628F dynamic and static strain test and analysis system was used for collecting data. Fig. 7 depicts the loading and measuring device.

2.2.2 Measurement Point Arrangement and Measurement Content

As indicated in Fig. 8a, displacement gauges were placed at the center of the bottom beam, 1/3 height and 2/3 height of the frame column. For the purpose of measuring the stress–strain data of the hoop and longitudinal reinforcement, the strain gauges were arranged as seen in Fig. 8b with a single-sided symmetric arrangement. For frame columns, strain gauges were placed at the bottom, 1/3 height, 2/3 height, and top of the column, respectively. For frame beams, strain gauges were installed close to the nodes.

In this test, the 3D-printed concrete wall frame monolithic structural specimens were measured for the following elements:

(1) Displacement and horizontal load upon loading.
(2) Lateral displacement of the specimen.
(3) Stress and strain of longitudinal and hoop reinforcement of frame beam and frame column.
(4) Crack development and damage distribution.

The horizontal load at the loading point could be read in the operating system of the MTS actuator. The displacement at the loading point was the MTS actuator data minus the displacement gauge reading at the center of the bottom beam. The TESTER collector gathered the strain data from the strain gauges. The crack development was traced with a marker, and the loading amplitude was also indicated.

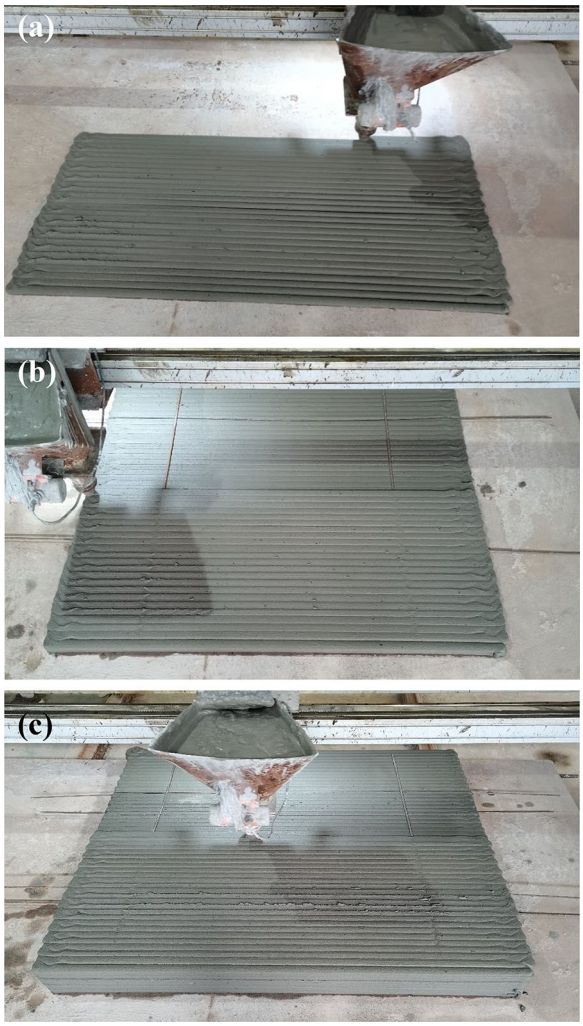

Fig. 4 Physical view of solid wall

2.2.3 Loading Plan

To evaluate the mechanical characteristics of the specimen under various displacement angles, the test was loaded by displacement control and constructed in accordance with the pertinent standard "Regulations for Seismic Test Methods for Buildings" (JGJ101-96), preloading and formal loading were the two stages of the test:

(1) Pre-loading stage: Pre-loading adopts ± 0.5 mm displacement amplitude to check the functionality of the strain gauges, wiring, equipment and other components. To apply load to the top of the frame column through the loading beam, two hydraulic jacks were used on either side of the frame column. The axial pressure ratio of 0.1 was selected for the test.

(2) Formal loading stage: Take the load–displacement curve at the obvious inflection point as the yielding point, the displacement amplitude corresponding to each displacement angle is cycled once before the specimen is yielded. After the specimen yielded, the displacement amplitude associated with each displacement angle was cycled three times. The test was continued until the bearing capacity of the specimen fell below 85% of the peak load, or the specimen was damaged and could no longer support the load. Each stage is cycled once when the displacement angles were 1/1000, 1/750, 1/600, 1/500, 1/400, 1/350, 1/300, 1/275, 1/250, 1/225. Each stage is cycled three times when the displacement angles were 1/200, 1/175, 1/150, 1/125, 1/110, 1/100, 1/90, 1/80, 1/70, 1/60, 1/50, 1/40, 1/35, 1/30, 1/25, and 1/20. Fig. 9 depicts the loading system.

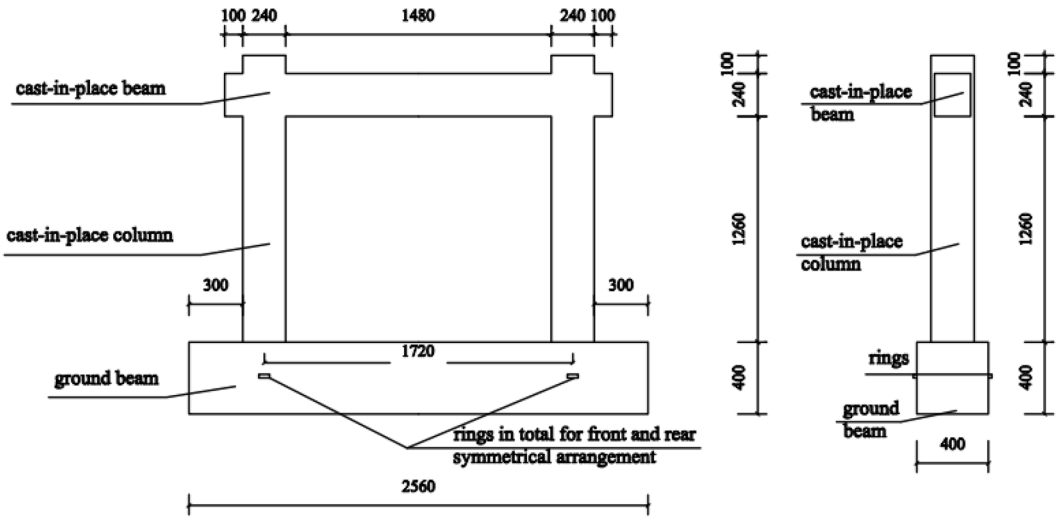

Fig. 5 Dimension diagram of frame (mm)

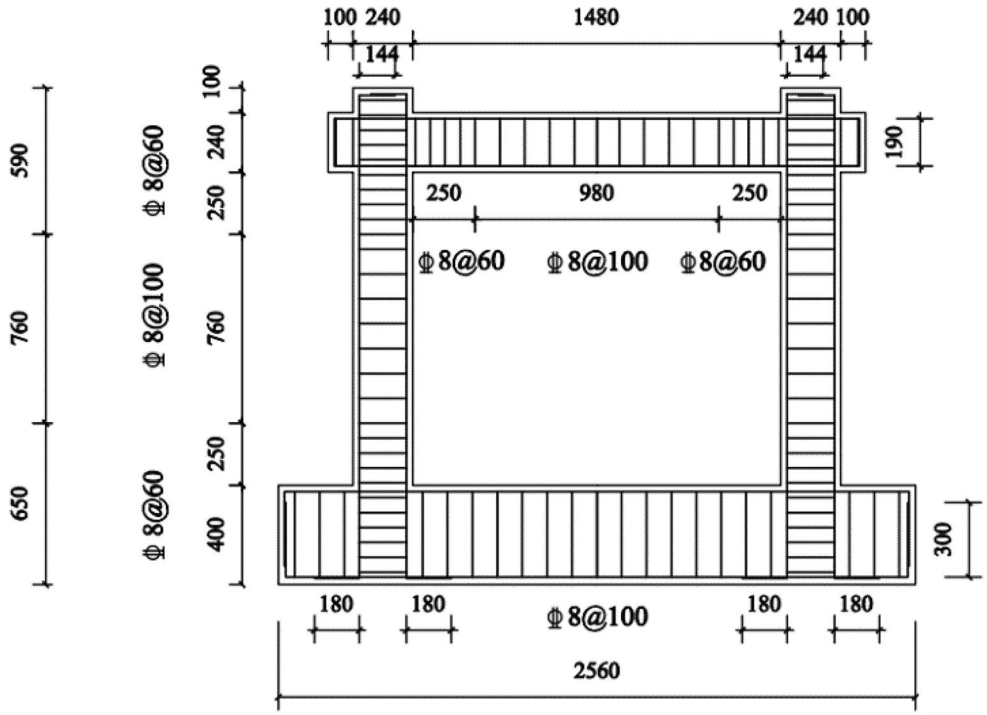

Fig. 6 Reinforcement of cast-in-place frame (mm)

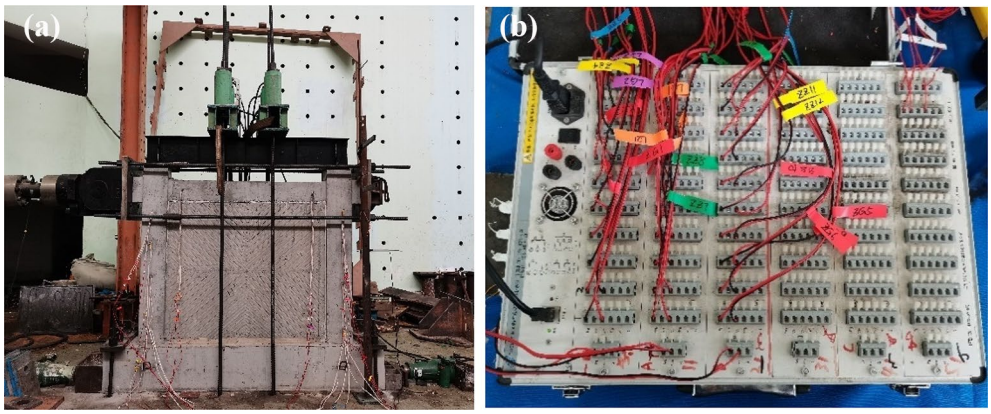

Fig. 7 Test setup diagram. **a** Loading device. **b** Measuring device

3 Material Properties

3.1 Concrete Materiality Test

The 3D-printed concrete strips created by stacking have weak adhesive layers between them (Ge et al., 2017, 04; Sanjayan et al., 2018), which results in mechanical anisotropy in the printed concrete components (Le et al., 2012, 3; Sanjayan et al., 2018; Zhang et al., 2021b, 1). In order to explore the impact of bonding between 3D-printed concrete strips on the mechanical properties of concrete, a concrete beam printed and molded with strips and three 150 mm × 150 mm × 150 mm cubic test blocks directly cast and molded with the printed concrete material in the mold were fabricated, respectively. In addition, three blocks made of C35 concrete measuring 150 mm × 150 mm × 150 mm cubic C35 were also cast. The cured concrete beam was divided into 18 150 mm × 150 mm × 150 mm cubic test blocks in groups of three, and the compressive strength test and splitting tensile strength test were performed on the concrete test blocks in X, Y and Z directions, respectively. (The

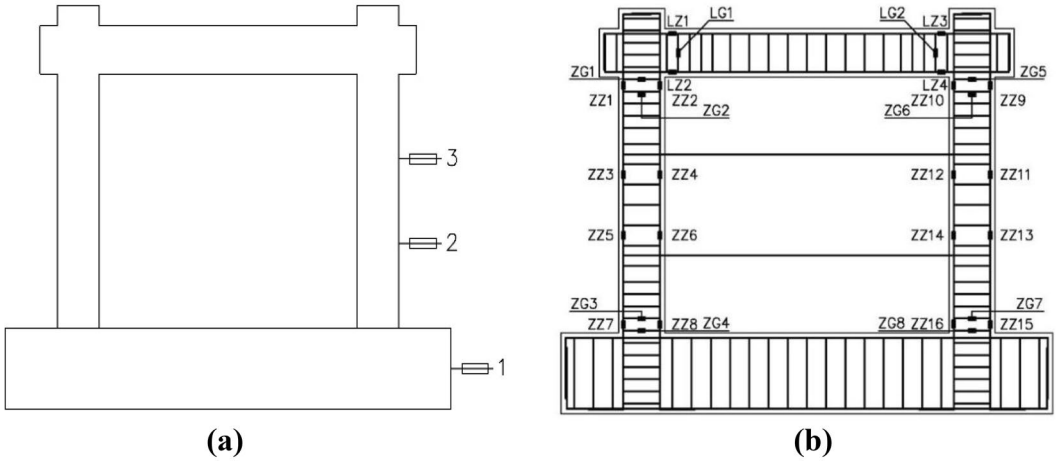

Fig. 8 Measurement point layout. **a** Schematic diagram of displacement gauge arrangement. **b** Layout of strain gauges

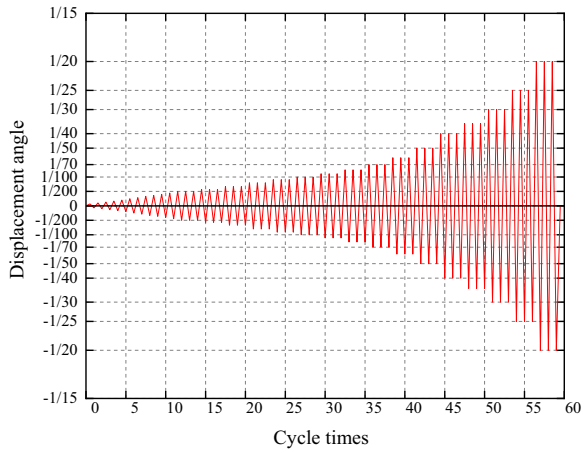

Fig. 9 Loading system

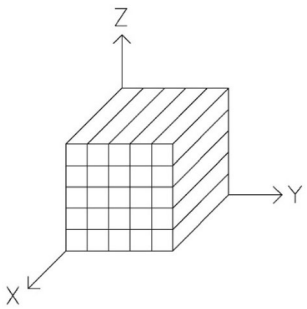

Fig. 10 Schematic diagram of the printing direction and the corresponding loading surface

standard specimen for testing the compressive strength of a concrete cube is a cube specimen with a side length of 150 mm (GB/T 50081-2019).) Fig. 10 displays the specimen printing directions and the matching loading surfaces. Table 1 displays the aggregate size and mortar makeup of the printed concrete. Table 2 displays the outcomes of the three-way compressive strength tests of the printed concrete specimens. Table 3 displays the outcomes of the splitting tensile strength test performed on the printed concrete specimens. Table 4 displays the test findings and compares the average cubic compressive strengths of three C35 concrete specimens and three 3D-printed concrete specimens that were cast and molded in molds.

Table 1 The aggregate size and mortar composition of the printed concrete

Material	Sulphate cement	Medium sand	Water	Polypropylene fiber	Polycarboxylate superplasticizer
Quality (kg/m^3)	700	600	260	2	6

3.2 Rebar Material Properties Test

The yield strength, ultimate strength, and modulus of elasticity of the steel bars were examined during the test, which was conducted in accordance with "Metallic materials-Tensile testing-Part 1: Method of test at room temperature" (GB/T 228.1-2010). Table 5 displays the mechanical characteristics of the reinforcing bars.

4 Test Procedure and Phenomenon

4.1 Specimen 1

The vertical force exerted at the top of the column is 96.192 kN since the axial pressure ratio is 0.1.

When the displacement angle $\theta = 1/150$ ($\Delta = 9.20$ mm), the column body appeared with multiple bending cracks, bending shear diagonal cracks, in which the cracks at 1/3 height and 1/2 height of the left column have extended

Table 2 Three-way compressive strength of 3D-printed concrete specimens

Number	Peak pressure (kN)	Pressure-bearing area (mm^2)	Compressive strength (MPa)	Average compressive strength (MPa)	Standard deviation
X-1	908	150×149	40.63	39.65	1.19
X-2	900	151×150	40.00		
X-3	851	149×149	38.33		
Y-1	636	151×149	28.27	28.16	1.07
Y-2	652	150×149	29.17		
Y-3	596	148×149	27.03		
Z-1	730	150×148	32.88	30.40	2.50
Z-2	685	151×149	30.45		
Z-3	619	149×149	27.88		

Table 3 Three-way splitting tensile strength of 3D-printed concrete specimens

Number	Peak pressure (kN)	Pressure-bearing area (mm^2)	Splitting tensile strength (MPa)	Average splitting tensile strength (MPa)	Standard deviation
X-1	64.51	150×150	1.83	1.77	0.074
X-2	60.12	151×150	1.69		
X-3	62.98	150×149	1.80		
Y-1	66.57	150×150	1.88	1.77	0.11
Y-2	58.96	150×151	1.66		
Y-3	62.15	151×150	1.76		
Z-1	112.31	149×150	3.20	3.22	0.11
Z-2	118.12	149×151	3.34		
Z-3	110.53	150×150	3.13		

Table 4 Average cubic compressive strength of poured test blocks f_{cu}

Specimen material	C35 fine stone concrete	3D-printed concrete
Number 1(MPa)	38.27	46.27
Number 2(MPa)	35.42	42.49
Number 3(MPa)	36.50	45.42
Cube compressive strength average (MPa)	36.73	44.72
Standard deviation	1.44	1.98

Table 5 Mechanical properties of reinforcing steel materials index

Reinforcing steel grade	Straight reinforcement bars (mm)	Yield strength (MPa)	Ultimate strength (MPa)	Modulus ($\times 10^5$Mpa)
HRB335	6	431	563	2.05
HRB400	6	466	627	2.02
	8	481	630	2.03
	12	485	641	1.95
	20	452	595	1.88

to the wall–column junction. A crack appeared at the junction of the left wall column and extended obliquely to the wall after cyclic loading of the displacement amplitude corresponding to this displacement angle. However, there was no audible crack sound. When the displacement angle $\theta = 1/110(\Delta = 12.55$ mm), the specimen gave way and started to cycle three times per stage. The left and right corners are broken and joined to the base of the column. A loud noise and a sudden widening of the crack on the right wall occurred when the displacement angle reached $\theta = 1/60$ ($\Delta = 23.00$ mm), at which point it ultimately pierced through the front and back. At this point, the original oblique cracks on both sides of the wall had extended to the bottom. The reinforcement was broken off and exposed at the bottom of the left and right columns where the concrete had spalled off. When the displacement angle $\theta = 1/40$ ($\Delta = 34.50$ mm), the original crack widened quickly, adding new cracks obliquely to the left in the right corner and the central part of the wall, and the cracks on the right side of the specimen quickly spreading to the bottom of the node. The bearing capacity of the specimen was reduced to less than 85% of the peak load, and the test ended. Specimen 1 ultimately displayed shear damage, and Fig. 11 depicts the damage

Fig. 11 Detailed drawing of the final damage pattern of Specimen 1. **a** Overall crack development on the front side of the specimen. **b** Left column bottom damage phenomenon. **c** Right column bottom damage phenomenon

pattern diagram (Δ is the horizontal displacement of the component).

4.2 Specimen 2

The vertical force exerted at the top of the column is 96.192 kN since the axial pressure ratio is 0.1.

At the 2/3 height of the right column and the 1/3 height of the two columns, many bending fractures extending to the wall–column junction occurred when the displacement angle reached $\theta = 1/250$ ($\Delta = 5.64$ mm). At the 1/2 height of the left column, numerous bending cracks that extended to the junction of the wall column were visible at the displacement angle $\theta = 1/150$ ($\Delta = 9.40$ mm). The wall's left and right corners developed cracks. The specimen yielded when the displacement angle $\theta = 1/110$ ($\Delta = 12.82$ mm), and three cycles per stage were started. Accompanied by a cracking sound, the oblique crack of the wall continued to extend rapidly, and the original oblique crack of the right wall extended to the center of the wall. At the displacement angle $\theta = 1/40$ ($\Delta = 35.25$ mm), the diagonal crack that was related to the wall column penetrated front to back, and a large piece of concrete spalled off at this crack, resulting in the exposure of reinforcement. The concrete at the bottom of the left and right column spalled off in large pieces, and the reinforcement at the bottom of both columns was sheared off and exposed. When the displacement angle $\theta = 1/35$ ($\Delta = 40.29$ mm), the specimen emitted a loud noise. The test ended when the bearing capacity of the specimen dropped to less than 85% of the peak load due to the vertical cracks along the wall–column junction, which caused out-of-plane dislocation. Specimen 2 was eventually revealed to have shear damage, and Fig. 12 depicts the damage mode diagram.

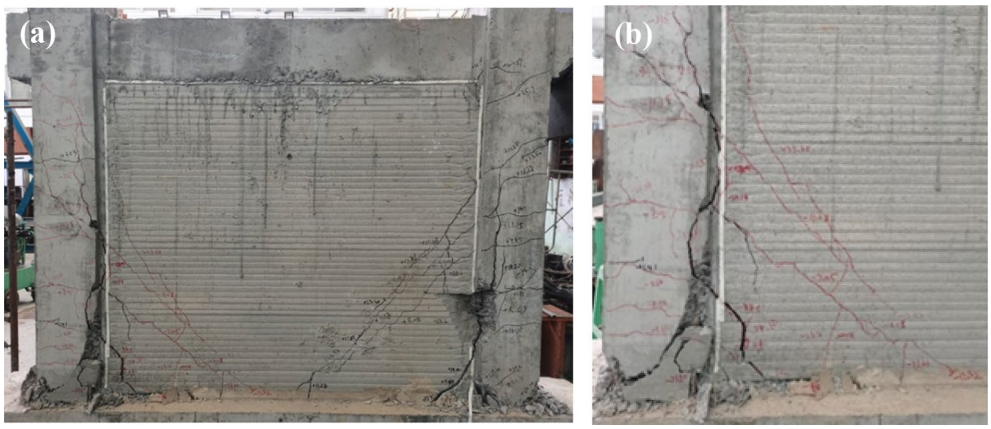

Fig. 12 Detailed drawing of the final damage pattern of Specimen 2. **a** Overall crack development at the back of the specimen. **b** Damage phenomenon at the bottom of the column

4.3 Specimen 3

The vertical force exerted at the top of the column is 96.192 kN since the axial pressure ratio is 0.1.

The inside of the beam–column joints split at the location, and bending cracks occurred at the bottom of both columns after the displacement angle reached $\theta = 1/275$ ($\Delta = 5.02$ mm). When the displacement angle $\theta = 1/110$ ($\Delta = 12.55$ mm), the specimen yielded, starting three cycles per stage. The concrete at the foot of the column developed cracks, while the body of the column had little bending and extending fissures. When the displacement angle $\theta = 1/60$($\Delta = 23.00$ mm), there were bending cracks and bending-shear diagonal cracks at 2/3 of the column. At the displacement angle $\theta = 1/50$ ($\Delta = 27.60$ mm), bending cracks appeared at both ends of the beam and the concrete at the bottom of the two columns began to fall. When the displacement angle $\theta = 1/25$ ($\Delta = 55.20$ mm), the cracks on the inner side of the node kept up extending upward diagonally and were accompanied by concrete mass spalling. The concrete at the bottom of the column was spalling off in large pieces, and the hoop reinforcement at the foot of the column was visible. At the displacement angle $\theta = 1/20$ ($\Delta = 69.00$ mm), the bearing capacity of the specimen fell to less than 85% of the peak load, and the test was terminated. Specimen 3 eventually manifested as frame column bending damage, and Fig. 13 depicts the damage pattern diagram.

5 Results and Discussion

5.1 Column Longitudinal Reinforcement Strain

Fig. 14 depicts the relationship between the strain of column longitudinal bars at various heights and the inter-story displacement angle when each inter-story displacement angle is loaded to the positive (push) maximum displacement. The column's base serves as the origin of elevation for the vertical axis, which shows the height of the strain gauges mounted at heights of 50 mm, 400 mm, 850 mm, and 1200 mm above the column's body. Table 6 displays the data table of a single longitudinal strain for the left column.

The following may be observed from the comparison graphs, which show how the aforementioned data were displayed against one another at various heights:

(1) The maximum strains of column longitudinal reinforcement in all specimens were located at the bottom of the column, and the damage at the bottom of the column occurred relatively early. Since the bottom of the column was subjected to the joint action of bending moment and shear force in the meanwhile, and the stiffness of the ground beam was greater compared with that of the frame beam, the ground beam had a stronger restraining effect on the column, causing a greater strain on the column bottom longitudinal reinforcement.

(2) The strain of the top longitudinal reinforcement and the strain of the bottom longitudinal reinforcement were not significantly different during the elastic stage. But once the elastoplastic stage began, the strain of the bottom longitudinal reinforcement started to rise considerably more quickly than the top longitudinal reinforcement, eventually reaching a level that is roughly twice that of the top of the column. Additionally, when the displacement angle increased, the anti-bending point gradually shifted upward, and a sizable force was applied to the column's lower portion.

(3) The maximum strain of the bottom longitudinal bars of Specimen 3 was much smaller compared to Specimens 1 and 2 because the 3D-printed concrete walls significantly increased the overall stiffness of the specimens. In addition, the inflection point of Specimen 3 was relatively close to the middle of the column as there was no wall to restrain it in this specimen. Compared with Specimen 2, Specimen 1 was less stiff, so the column had to support a bigger proportion of

Fig. 13 Detail of the final damage pattern of Specimen 3. **a** Overall crack development on the front of Specimen 3. **b** Inner penetration joint of the node. **c** Damage phenomenon at the bottom of the column

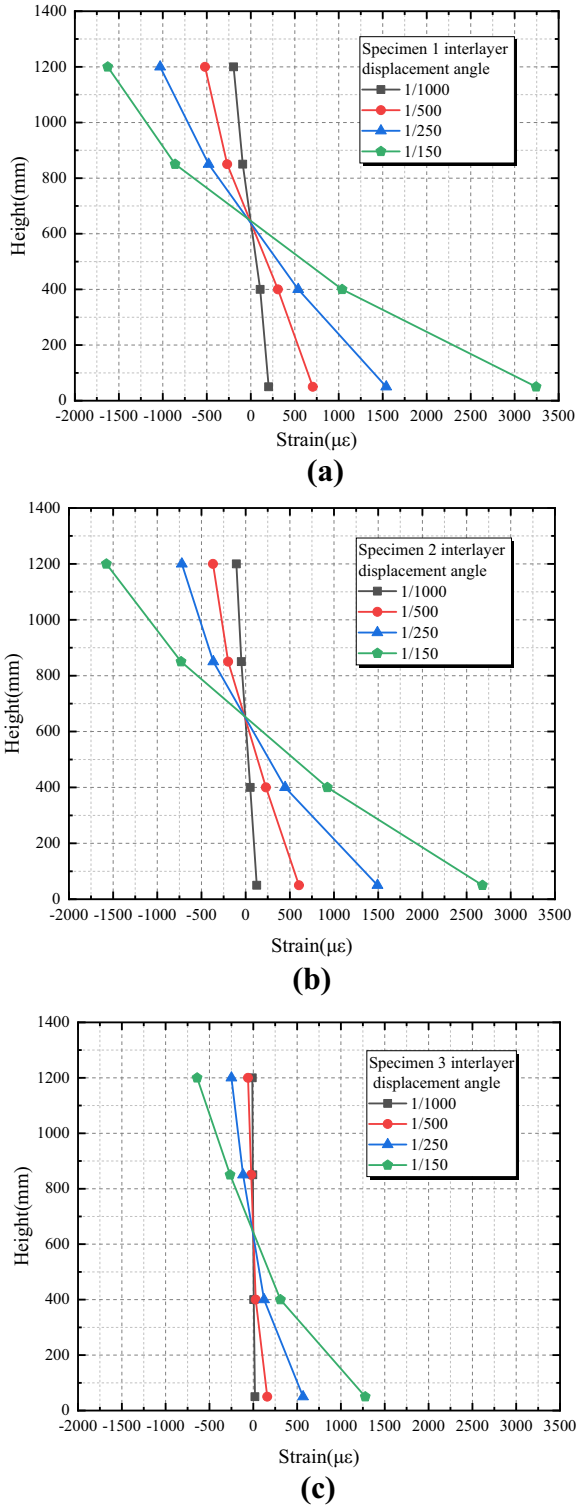

Fig. 14 Strain of column longitudinal reinforcement under different inter-story displacement angles: **a** Specimen 1, **b** Specimen 2, **c** Specimen 3

Table 6 Column longitudinal reinforcement strain data table ($\mu\varepsilon$)

H (mm)	φ			
	1/1000	1/500	1/250	1/150
(a) Specimen 1 column longitudinal bar strain data ($\mu\varepsilon$)				
1200	−195.28	−520.49	−1030.52	−1626.37
850	−91.95	−267.83	−478.34	−860.58
400	106.31	308.15	539.2	1038.73
50	203.58	704.32	1540.37	3244.72
(b) Specimen 2 column longitudinal bar strain data ($\mu\varepsilon$)				
1200	−105.07	−370.27	−722.16	−1576.02
850	−49.4	−198.4	−366.28	−730.58
400	50.91	230.05	446.05	924.6
50	125.3	603.58	1492.18	2680.47
(c) Specimen 3 column longitudinal bar strain data ($\mu\varepsilon$)				
1200	−10.87	−59.46	−250.01	−640.73
850	−4.54	−23.84	−116.29	−264.28
400	5.22	27.48	123.57	309.7
50	19.11	159.46	567.93	1278.45

horizontal load, which led to much greater column longitudinal deformation in Specimen 1 than in Specimen 2.

5.2 Hysteresis Curves

The displacement ductility, stiffness degradation, strength degradation, energy dissipation capacity, residual deformation, and other indicators of the specimens are all reflected in the hysteresis curves during cyclic loading. Fig. 15 displays the hysteresis curves of each specimen, where n is the specimen axial pressure ratio.

The following conclusions can be drawn from the figures:

(1) The hysteresis curve of Specimen 3 has a shuttle-like form. The residual deformation at the late loading stage is enormous with a full curve, and large ultimate displacement angle, possessing good ductility and energy dissipation capacity. The stiffness degradation is gradual and there is no visible dramatic change. Up to the second and third cycles in the last stage, the load capacity grows gradually before abruptly decreasing. The damage mode is consistent with the design concept of "strong column and weak beam".

(2) The slope of the cut line of the hysteresis curve at the beginning of loading of Specimens 1 and 2 was larger, and when the slope of the cut line started to fall with a slow falling rate and the stiffness of the specimen did not change significantly at this point, and the bearing

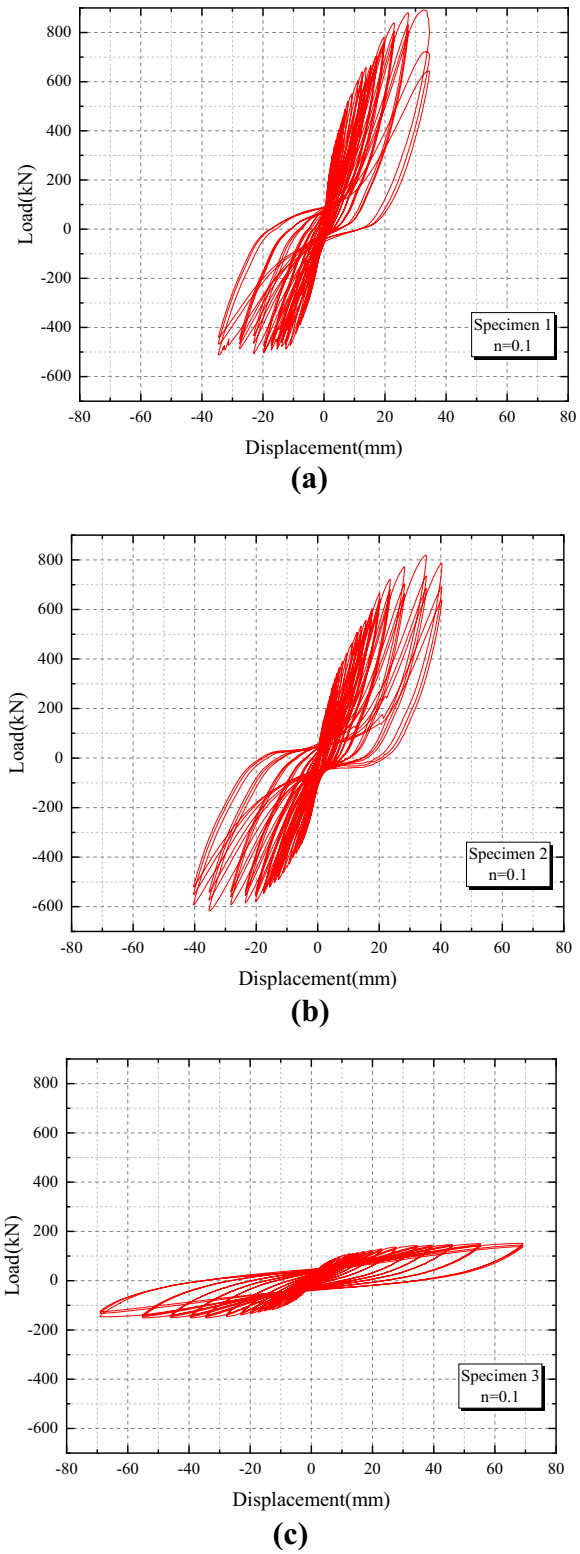

Fig. 15 Specimen hysteresis curve: **a** Specimen 1, **b** Specimen 2, **c** Specimen 3

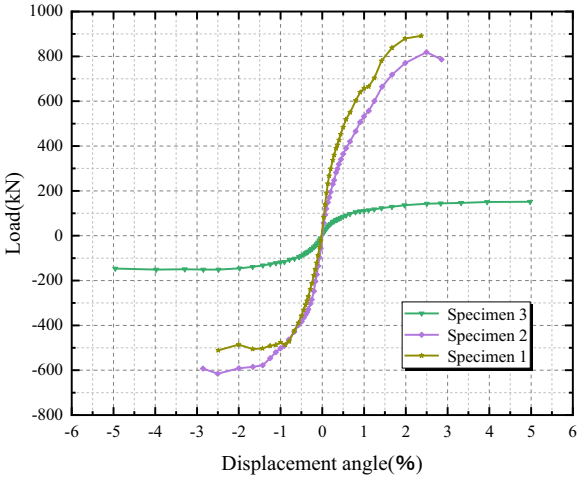

Fig. 16 Specimen skeleton curve

capacity also gradually increased. Although the two specimens slipped to different degrees when the specimen yielded and the hysteresis curve depicted various degrees of pinching, all of these deformations are represented as shear damage, and the overall shear deformation was greater.

(3) The inclusion of the wall drastically altered the overall performance of the specimen compared to Specimen 3. Specimen 1 slipped more, and the wall rigidity of this specimen was decreased by the hollow section of the wall. At the late stage of loading, there were more cracks within the column as well as the rapid development of wall cracks, which lowered the shear capacity of the specimen and increased the shear deformation. In the last stages of loading, Specimen 2 had a considerable reduction in shear capacity that extended from the corner of the wall to both sides of the column with a large slip.

5.3 Skeleton Curves

The envelope connected by the peak load points of the first cycle of each stage was referred to as the skeleton curve. Fig. 16 displays the skeleton curve of each specimen. The cracking load P_{cr} was the load value corresponding to the initial crack in the specimen. The energy equivalence approach was used to calculate the equivalent yield point. P_{max} was the peak load of the specimen. The value at which the horizontal load was downloaded to 85% of the peak load, or the load value at which the specimen was damaged, was the ultimate load P_u. When Specimen 3 was loaded forward to the last level, the load was still not downloaded to 85% of the peak load P_{max}, the maximum value of the load at the last level in the forward direction is taken as the ultimate load P_u.

A comparative analysis of the specimen skeleton curves and characteristic points shows that:

(1) Specimen 1 exhibited a rapid growth of peak load when the displacement angle was small. However, when $\theta=1/60=1.67\%$ ($\Delta=23.00$ mm), the oblique main crack of the wall column had been penetrated before and after the wall section due to the small stiffness of the wall. Following that, the column carried the majority of the horizontal load, and the bearing capacity kept increasing quickly. When the displacement angle $\theta=1/50=2\%$ ($\Delta=27.60$ mm), more cracks appeared in the column body and the bearing capacity of the column gradually decreased. After reaching the final level of displacement angle $\theta=1/40=2.5\%$ ($\Delta=34.50$ mm), the bearing capacity of the column rapidly declined to below 85% of the peak load after two cycles.

(2) The peak load curve of Specimen 2 followed the same general pattern as Specimen 1. When the displacement angle reached $\theta=1/60=1.67\%$ ($\Delta=23.50$ mm), the main oblique crack of the wall column just cracked, indicating that the wall column functioned well together and the bearing capacity could still support a high rise. When the displacement angle was equal to $\theta=1/50=2\%$ ($\Delta=28.20$ mm), the main crack had penetrated before and after. At the displacement angle $\theta=1/40=2.5\%$ ($\Delta=35.25$ mm), the column bottom damage occurred, leading to the last level of bearing capacity declining rapidly to below 85% of the peak.

(3) The bearing capacity of Specimen 3 changed consistently as it developed. However, the peak load of Specimen 3 under the same displacement angle was significantly lower than that of Specimens 1 and 2, showing that the addition of the wall increases the peak load of the specimen.

5.4 Energy Dissipation Capacity

The energy dissipation capacity of a structure or component under earthquake action was one of the crucial seismic performance indicators. In this paper, the cumulative energy dissipation E_a and the equivalent viscous damping coefficient h_e were used to assess the energy dissipation capacity of the specimens. The cumulative energy dissipation E_a was the cumulative value of the seismic energy absorbed throughout the loading process, i.e., the sum of the enclosed area of the hysteresis loop (Tang, 1989). The capability for dissipating energy increases with the corresponding viscous damping coefficient he. The calculation formula is as follows (Jacobsen, 1930):

$$h_e = \frac{1}{2\pi} \cdot \frac{S_{ABC} + S_{CDA}}{S_{OBE} + S_{ODF}},$$

where h_e, the equivalent viscous damping coefficient; $S_{ABC} + S_{CDA}$, the uniperiodic hysteresis energy dissipation; $S_{OBE} + S_{ODF}$, the energy absorbed by the ideal elastic structure when the same displacement is reached (Zheng et al., 2017, 09) Figure 17 depicts the calculation of the viscous damping coefficient (Li, 2019).

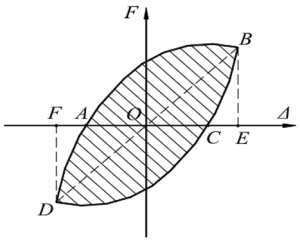

Fig. 17 Schematic diagram of the calculation of the viscous damping coefficient (Li, 2019)

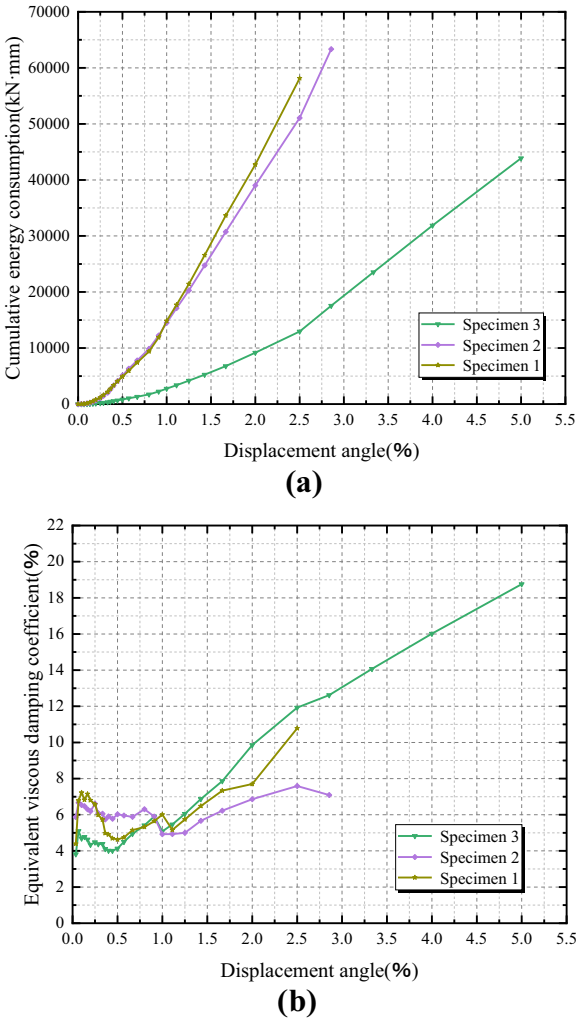

Fig. 18 Specimen energy consumption capacity. **a** Cumulative energy consumption curve of three specimens. **b** Equivalent viscous damping coefficient curve

Fig. 18 displays the cumulative energy dissipation curve and equivalent viscous damping coefficient curve of each specimen.

The following conclusions can be drawn from the analysis of Fig. 18:

(1) Each specimen's cumulative energy dissipation curve developed in three stages. The first stage occurred before cracking, the specimen was in the elastic working stage, and the current stage saw very little residual deformation. The cumulative energy dissipation was negligible. The second stage was after cracking and before destruction, the specimen entered the elastic–plastic working stage, cracks were continuously added and expanded, and the accumulated energy consumption grew steadily. In the third stage, the crack development of the specimen was accelerated, the damage noticeably increased, and the accumulated energy consumption grew rapidly as the specimen was on the verge of being destroyed.

(2) After cracking and yielding, each specimen's corresponding viscous damping coefficient developed in two decreasing stages. The equivalent viscous damping coefficient fluctuated slightly depending on how each specimen's crack developed in the first case, and it climbed continuously after that. The second time was the sharp decrease that occurred after the specimen yielded, and the subsequent acceleration of the rise in the equivalent viscous damping coefficient reflected the rapid increase of its energy dissipation capacity.

(3) The equivalent viscous damping coefficient curve of Specimen 2 was located at the bottom, but the final cumulative energy dissipation was the highest due to the relatively large damage displacement angle. Both curves of Specimen 1 were located above Specimen 2 after yielding, indicating that its energy dissipation capacity was relatively better at the same displacement angle. Specimen 3 had a good energy dissipation capacity and a big damage displacement angle, but it dissipated less energy cumulatively than the other specimens under the same displacement angle.

6 Conclusion

According to the damage morphology of the above three specimens and the comparative analysis of the seismic performance, the 3D-printed concrete wall frame monolithic structure specimens exhibited the following seismic performance:

(1) Due to the addition of printed walls, the cast-in-place frame printed concrete wall structure (Specimens 1 and 2) increased the stiffness and load-bearing capacity of the specimen. It also caused the bottom longitudinal reinforcement of the column to deform more, shifting the column's reverse bending point upward. However, the increased stiffness reduced the ductility of the structure and made it susceptible to cracking at the wall–column nodes. Both Specimens 1 and 2 had extensive shear-type damage.

(2) The cumulative energy dissipation curves and equivalent viscous damping coefficient curves of the specimens revealed that the components with printed walls (Specimens 1 and 2) had greater cumulative energy dissipation than the frame members (Specimen 3), proving that the addition of the walls improved the seismic energy dissipation capacity of the frame.

(3) The equivalent viscous damping coefficient for the same displacement angle was higher for the hollow wall because its stiffness was lower than that of the solid wall. Hollow walls had slightly lower peak loads and cumulative energy dissipation than solid walls. The seismic performance of the members, however, is generally not significantly impacted by the wall sections.

(4) The printed concrete walls in this test failed to fully participate in the seismic energy dissipation of the structure, and further coordination of the stiffness between the printed concrete walls and the cast-in-place frame is necessary to achieve higher ductility.

Acknowledgements
The authors gratefully acknowledge the financial support of the National Key R&D Program of China (2018YFC0705800).

Author contributions
All authors contributed substantially to all aspects of this article. All authors read and approved the final manuscript.

Funding
This work is financially supported by the National Key R&D Program of China under 2018YFC0705800.

Availability of data and materials
All data used during the study appear in the submitted article.

Declarations

Competing interests
The authors declare that they have no conflict of interest.

Received: 4 November 2022 Accepted: 11 June 2023
Published online: 08 November 2023

References

Alec. (2016). WinSun 3D prints two gorgeous concrete Chinese courtyards inspired by ancient Suzhou gardens. http://www.3ders.org/articles/20160331-winsun-3d-prints-two-gorgeous-concrete-chinese-courtyards-inspired-by-the-ancient-suzhou-gardens.html

Frearson, A. (2018). Eindhoven to build "world's first" 3D-printed houses that people will live inside. https://www.dezeen.com/2018/06/04/eindhoven-university-technology-project-milestone-3d-printed-concrete-houses/

Gallow, L. (2022). What it's really like to live in a 3D-printed home. https://www.dwell.com/article/what-its-really-like-to-live-in-a-3d-printed-home-bf0fa07f

Ge, J., Ma, R. Q., Miao, D. M., et al. (2017). Experimental study of interlayer bonding performance of 3D printed construction materials. *Building Structure, 47*(04), 49–52. https://doi.org/10.19701/j.jzjg.2017.04.010. in Chinese.

Jacobsen, L. (1930). Steady forced vibrations as influenced by damping. *Trans Asme, 52*, 169–178.
Keighran, M. (2022). A Dutch couple are the first tenants of this boulder-shaped 3D-printed home. https://www.dwell.com/article/3d-printed-house-project-milestone-f1c6f137
Koslow, T. (2016). DUS Architects constructs 3D Printed "Urban Cabin" in Amsterdam. https://3dprint.com/147687/dus-architects-urban-cabin/
Le, T. T., Austin, S. A., Lim, S., Buswell, R. A., Law, R., Gibb, A. G. F., & Thorpe T. (2012). Hardened properties of high-performance printing concrete [Article]. *Cement and Concrete Research, 42*(3), 558–566. https://doi.org/10.1016/j.cemconres.2011.12.003
Li, B. (2019). Research on seismic performance test and calculation method of assembled monolithic fiber recycled concrete shear wall. [Ph., Xi'an University of Architecture and Technology:Xi'an,China, 2019.]. (in Chinese)
Lin, X. Q., Huo, L., Su, K., et al. (2021). Construction key technology of 3D printed two-story office for in-situ construction. *China Building Materials Science & Technology, 30*(03), 70–78. in Chinese.
Liu, Z., Li, M., Weng, Y., Wong, T. N., & Tan, M. J. (2019). Mixture design approach to optimize the rheological properties of the material used in 3D cementitious material printing. *Construction and Building Materials, 198*, 245–255. https://doi.org/10.1016/j.conbuildmat.2018.11.252
Mechtcherine, V., Grafe, J., Nerella, V. N., Spaniol, E., Hertel, M., & Füssel, U. (2018). 3D-printed steel reinforcement for digital concrete construction-Manufacture, mechanical properties and bond behaviour. *Construction and Building Materials, 179*, 125–137. https://doi.org/10.1016/j.conbuildmat.2018.05.202
Ministry of Construction of the People's Republic of China. (1997). JGJ 101-96 Specification of Testing Methods for Earthquake Resistant Building (in Chinese).
Ministry of Construction of the People's Republic of China. (2015). GB 50010-2010 Code for design of concrete structures (in Chinese).
Ministry of Housing and Urban-Rural Development of the People's Republic of China. (2019). GB/T50081-2019 Standard for test methods of concrete physical and mechanical properties (in Chinese).
Molitch-Hou, M. (2016). 400-square-meter villa 3D printed onsite in just 45 days. https://www.engineering.com/story/400-square-meter-villa-3d-printed-onsite-in-just-45-days
Panda, B., Paul, S. C., Mohamed, N. A. N., & Tay Y. W. D. (2018). Measurement of tensile bond strength of 3D printed geopolymer mortar. *Measurement, 113*, 108–116. https://doi.org/10.1016/j.measurement.2017.08.051
Sanjayan, J. G., Nematollahi, B., Xia, M., & Marchment, T. (2018). Effect of surface moisture on inter-layer strength of 3D printed concrete [Article]. *Construction and Building Materials, 172*, 468–475. https://doi.org/10.1016/j.conbuildmat.2018.03.232
Tang, J. R. (1989). *Seismic resistance of reinforced concrete frame nodes*. Southeast University Press. in Chinese.
Tess. (2016). Dubai lays out regulations for 3D printed buildings. http://www.3ders.org/articles/20160714-dubai-lays-out-regulations-for-3d-printed-buildings.html
The Standardization Administration of the People's Republic of China. (2010). GB/T 228.1-2010 Metallic materials-Tensile testing-Part 1: Method of test at room temperature(in Chinese).
Yu, F. L. (2015). 3D-printed homes debut in Suzhou Industrial Park. *Housing Science, 35*(02), 60–61. https://doi.org/10.13626/j.cnki.hs.2015.02.016
Zhang, P. (2020). Experimental study on the compressive performance of 3D printed concrete walls. [Master, Southeast University:Nanjing,China, 2020.]. (in Chinese)
Zhang, Q., Du, C. X., Zhang, P., et al. (2021a). Study on the axial compression performance of 3D printed concrete walls. *Industrial Construction, 51*(06), 36–41. https://doi.org/10.13204/j.gyjzG20121501. in Chinese.
Zhang, Y., Zhang, Y., Yang, L., Liu, G., Chen, Y., Yu. S., & Du, H. (2021b). Hardened properties and durability of large-scale 3D printed cement-based materials. *Materials and Structures, 54*(1), 1–14. https://doi.org/10.1617/s11527-021-01632-x
Zheng, S. S., Zhang, Y. X., Huang, Y. G., Guan, Y., & Zheng, J. (2017). Experimental study on seismic performance of reinforced concrete frame beams under acid rain environment. *Journal of Building Structures, 38*(09), 20–27. https://doi.org/10.14006/j.jzjgxb.2017.09.003. in Chinese.

Publisher's Note

Yanan Fu MS student, Southeast University, Jiangsu, Nanjing, 211189, China.

Ying Zhang MS student, Southeast University, Jiangsu, Nanjing, 211189, China.

Lei Wu Associate Professor, Southeast University, Jiangsu, Nanjing, 211189, China